A RELATIVISTIC MONTE CARLO BINARY COLLISION MODEL FOR USE IN PLASMA PARTICLE SIMULATION CODES

by

R. J. Procassini, C. K. Birdsall, E. C. Morse,
and B. I. Cohen

Memorandum No. UCB/ERL M87/24

14 May 1987

A RELATIVISTIC MONTE CARLO BINARY COLLISION MODEL FOR USE IN PLASMA PARTICLE SIMULATION CODES

by

R. J. Procassini, C. K. Birdsall, E. C. Morse, and B. I. Cohen

ELECTRONICS RESEARCH LABORATORY

College of Engineering
University of California, Berkeley
94720

A RELATIVISTIC MONTE CARLO BINARY COLLISION MODEL FOR USE IN PLASMA PARTICLE SIMULATION CODES

by

R. J. Procassini, C. K. Birdsall, E. C. Morse, and B. I. Cohen

ELECTRONICS RESEARCH LABORATORY

College of Engineering
University of California, Berkeley
94720

A Relativistic Monte Carlo Binary Collision Model for Use in Plasma Particle Simulation Codes

R. J. Procassini, C. K. Birdsall and E. C. Morse
and
B. I. Cohen (Lawrence Livermore National Laboratory)

1. Introduction

Particle simulations of plasma physics phenomena employ far fewer particles than the systems which are being simulated, owing to the limited speed and memory capacity of even the most powerful supercomputers. In practice, a system containing as many as 10^{20} particles is studied with upwards of 10^4 simulation particles. If the simulation consists of point particles in a gridless domain, then the combination of the small number of particles in a Debye sphere and the possibility of zero-impact-parameter, large-angle scattering results in a significant enhancement of fluctuation phenomena such as collisions.

In contrast, a gridded simulation has finite-size particles, due to the weighting or interpolation of the particles onto the grid and vice versa for the forces. These finite-size particles are tenuous in nature, being able to pass through each other. Therefore the interparticle force does not become singular as the distance of separation of the particle midpoints goes to zero, as it does for point particles.[1] This means that the average scattering angle for finite-size particle interactions is much smaller than that for point particle interactions, hence the collisionality for finite-size particles is reduced relative to that for point particles.

Accommodating collisional processes in a simulation may be difficult because

of disparate time scales. A comparison of the relevant physical time scales of the system that is being simulated usually yields a large range of values. For instance, the grid-cell transit time is usually several orders of magnitude smaller than the $90°$ scattering time. Much of the physical phenomena of interest in the simulation are due to these long-time-scale collisional processes[2], but short-time-scale processes (such as particle bounce times in a mirror or tokamak) must be adequately resolved if the plasma dielectric response and the plasma potential are to be accurately determined. This leads to important constraints on the modeling of binary collisions in our electrostatic particle simulation code **TESS** (Tandem Experiment Simulation Studies).

In the following section we outline the physics and operation of the binary collision model within the electrostatic particle code. Section 3 presents the results of computer simulations of velocity space transport which were run to test the accuracy of the model. Finally, Section 4 discusses the timing statistics for the collision package relative to the other major physics packages in the code, as well as recommendations on the frequency of use of the collision package within the simulation sequence.

2. The Binary Collision Model

The binary collision model presented in this paper is fully relativistic, exclusive of radiation losses, and employs Monte Carlo techniques to simulate the scattering of plasma particles. It is similar in operation to the nonrelativistic model suggested by Takizuka and Abe.[3] Since the **TESS** code has only one spatial dimension (with three velocity components), it is not possible to simulate the details of Coulomb

scattering based upon impact parameters. However, it is possible to scatter particles through an angle which is chosen randomly from a distribution of angles. The mean scattering angle is zero and the width or variance of the distribution is a function of the particle charges, density, reduced mass and relative velocity, as well as the simulation timestep. Particles within a given spatial grid cell are scattered off of each other without regard for the distance between the midpoints of these finite-size particles. The model is designed to handle any combination of projectile and target particles: electron-electron (e-e), electron-ion (e-i, which is equivalent to i-e) and ion-ion (i-i) scattering.

The following is a step by step outline of the operations that are performed in the binary collision model:

Step 1 - The *absolute* indices for all the ions and electrons in a given grid cell are written into the two dimensional arrays $NIC(ipg, ig)$ and $NEC(ipg, ig)$ respectively, where ipg is the *gridwise* index of particles within the given grid cell and ig is the grid-cell index (ipg lies in the range $[0, Npg(ig)]$, where $Npg(ig)$ is the total number of ions or electrons in grid cell ig, and ig lies in the range $[1, Ng]$, where Ng is the total number of grid cells in the system). This process takes place in the particle mover routine (PUSHER).

Begin Grid Cell Loop $\qquad ig = 1 \ \ to \ \ Ng$

Step 2 - "Gather" the particle variables from the absolute index (permanent) particle arrays into temporary arrays which are of length $Npg(ig)$. This unvectorizable sorting process is required such that the particle loop described below can

4

be vectorized. This *software* vector-gather process is necessary since not all vector computers have *hardware* vector-gather-scatter capability.

Begin Particle Loop $ipg = 1$ *to* $Npg(ig)$ [Vectorizable]

Step 3 - The **TESS** code uses axial ($\hat{z}$ direction) momenta and magnetic moments to advance the particles. At this point, the magnetic moment of the particle is converted to a perpendicular (gyro) momentum via

$$\mathbf{p}_\perp = \sqrt{2mB_{ave}\mu} \tag{1}$$

The momentum components in the $\hat{x}$ and $\hat{y}$ directions of the incident particle (particle 1) are then calculated from the perpendicular momentum and a randomly chosen angle of gyration. The x-component of momentum for the target particle (particle 2) is set equal to the perpendicular momentum, while the y-component of momentum is set equal to zero, thereby giving a reference direction for the rotation discussed in the next step.

Step 4 - Rotate the coordinate system about the $\hat{y}$ axis such that the rotated $\hat{z}$ axis ($\hat{z}_r$) is aligned along the momentum vector for the target particle ($\mathbf{p}_2$) which lies in the x-z plane. This coordinate system rotation is shown in Figure 1.

Step 5 - Lorentz transform the binary particle system such that the target particle is then at rest ($\mathbf{p}_{2L} = 0$). This choice of reference frame for particle scattering has been inspired by the treatment of relativistic particle scattering presented in Jackson.[4] The center of mass (COM) reference frame was considered for use, but required a few more executable statements to set up. Therefore, in order to optimize the computational efficiency of the model, the target-particle-at-rest frame was chosen over the COM frame.
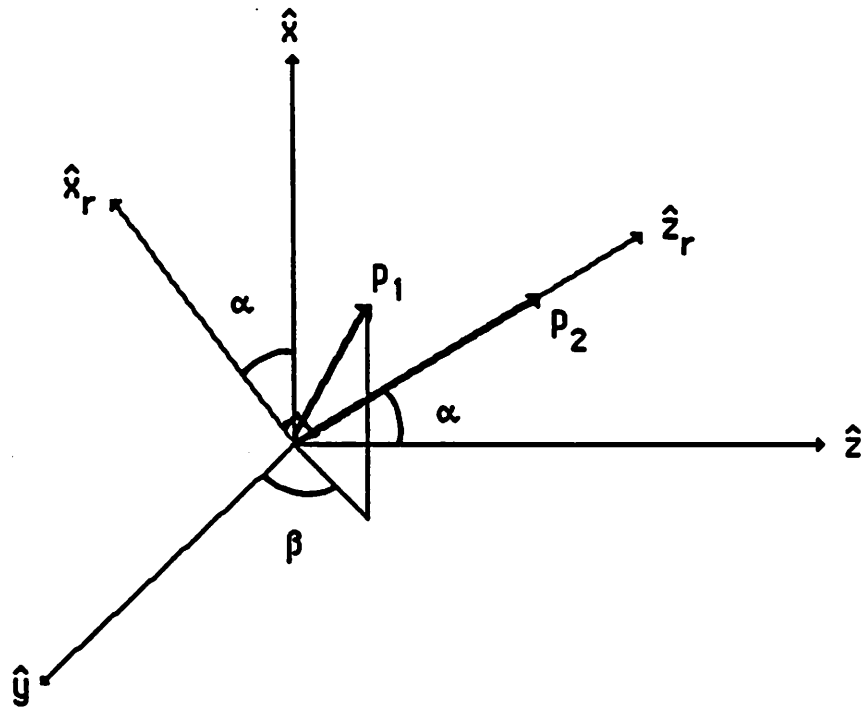
Figure 1. The rotation of the $\hat{z}$ axis to align the rotated $\hat{z}_r$ axis with the incident particle momentum vector (p_2).

Step 6 - Scatter the incident particle through a small angle. The polar COM scattering angle (θ') is chosen randomly from a distribution of angles which has a mean value of zero, and a width or variance which is given by

$$\langle \delta^2 \rangle = (\frac{m_1 v_{z_{th}}}{p_{cm}})^2 \frac{v_{z_{th}}}{v_{cm}} \frac{n_{loc}}{n_{ave}} \frac{N_{tc}}{N_{cp}} \nu \Delta t \qquad (2)$$

where p_{cm} and v_{cm} are the momentum and velocity of the center of mass in the target-particle-at-rest frame, m_1 is the mass of the incident particle, $v_{z_{th}}$ is the axial thermal velocity of incident particle in the initial reference frame, ν is the collision frequency specified as an input parameter, Δt is the simulation timestep and n_{loc}/n_{ave} is the ratio of the local to average target particle densities. The quantity N_{tc} is the number of timesteps between subsequent executions of the binary collision package, and N_{cp} is the number of binary collisions that each particle experiences each time the collision model is called. (The first of these input parameters allows one to increase the computational efficiency of the results by executing the model every N_{tc} timesteps, instead of every timestep. The second allows one to increase the statistical accuracy of the results, by increasing the number of collisions per particle for each call to the routine). This definition of the variance of the scattering angle distribution is due to Spitzer[5] as modified for relativity[4]. The azimuthal scattering angle is chosen randomly.

Step 7 - Calculate the change in momentum of the incident particle Δp_1 and the resultant momentum q_{1L} in the target-particle-at-rest frame. The polar scattering angle in this frame (θ_3) is obtained from the COM polar scattering angle (θ') via Equations 12.31, 12.50 and 12.54 of [4]. The energy lost by the incident particle

during the collision is given by Equation 12.55 of [4]. The scattering geometry in the target-particle-at-rest frame is shown in Figure 2.

Step 8 - Perform an inverse Lorentz transform to obtain the rotated frame and the momentum q_{1R}.

Step 9 - Perform an inverse rotation to arrive at the final state for the incident particle with momentum q_1.

Step 10 - Calculate the components of the scattered target particle momentum q_2 by enforcing momentum conservation on a component by component basis

$$q_2 = p_1 + p_2 - q_1. \tag{3}$$

This algorithm explicitly conserves the momentum of the scattered particle pair and implicitly conserves energy.

End Particle Loop

Step 11 - "Scatter" the collided values in the temporary particle arrays back into the absolute index (permanent) particle arrays. This unvectorizable process is the software vector-scatter process.

End Grid Cell Loop

The large, inner *particle loop* is vectorizable, but the vector-gather-scatter processes (Steps 2 and 11) are unvectorizable loops (except for machines which have hardware vector-gather-scatter capability) that are required in order for the particle loop to be vectorizable. In any given grid cell ig, the initial pair of particles to be scattered are chosen as follows. For like-particle scattering (e-e or i-i), the temporary arrays of length $Npg(ig)$ are split into two lists of equal length (for $Npg(ig)$
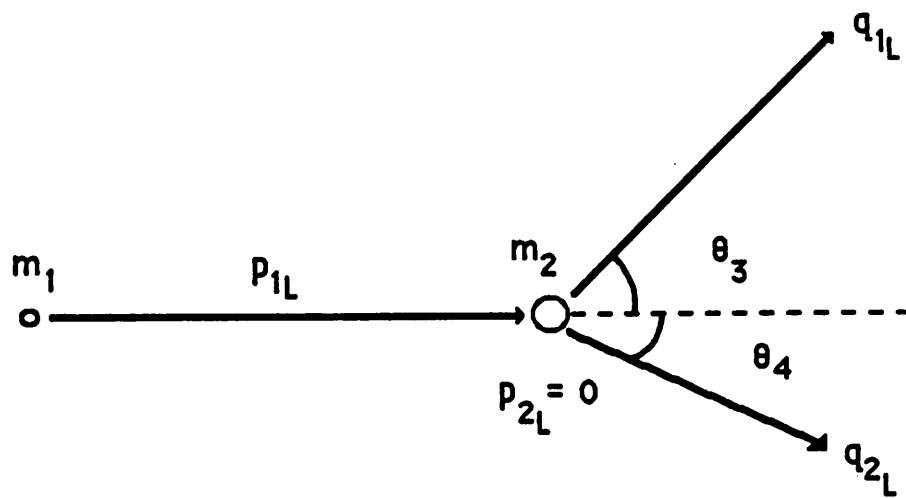
Figure 2. The scattering geometry in the target-particle-at-rest frame, showing the polar scattering angle of the incident particle (θ_3).

even) or two lists differing in length by one (for $Npg(ig)$ odd). For unlike-particle scattering (e-i), no subdivision of the temporary arrays (lists) is required. The starting location in the first list is taken as the first particle, while the starting location in the second list is chosen randomly. When the last particle in the second list has been scattered, the list "wraps around", such that the next particle to be scattered is the first particle in that list. If each particle in the grid cell is to be scattered more than once per execution of the collision package, the starting location in the second list is always chosen randomly. This helps to ensure that the same particle pairs are not used more than once for any execution of the collision package. This random selection of incident (test) and target (field) particle pairs has been shown[6] to be approximately equivalent to an integration of the field particle distribution function, if the time between execution of the collision package is much smaller than the effective 90° scattering time and if there are enough unique collision pairs to give decent statistical resolution of the local velocity distribution function.

3. Simulation Results of Plasma Relaxation Processes

In order to verify the accuracy of the binary collision model, several simulations were performed for various incident (test)and target (field) particle combinations, and different velocity distribution functions (beam and Maxwellian) in both the nonrelativistic and relativistic limits. These simulations used finite-size particles in a gridded domain, however the Poisson field solver and the spatial particle advance were disabled. Therefore, these simulations dealt only with velocity space transport of particles in a spatially uniform plasma.

Three types of plasma relaxation processes were studied: transverse diffusion, slowing down and energy loss. These proceses are discussed in depth in [5] and [7]. Each of these processes will be discussed in detail below. The number of simulation particles ($N_{sp} = 6400$) and initial particle density ($n_o = 100$) were the same for each simulation. The parameters that were different between simulations include the ion to electron mass ratio (m_i/m_e), the ion and electron temperatures ($T_{z_i}, T_{\perp_i}, T_{z_e}$ and $T_{\perp_e}$) and total number of timesteps (N_t). Since the spatial density of particles remained uniform during the simulations, the ratio $n_{loc}/n_{ave} = 1$. Furthermore, the collision package was executed each timestep ($N_{tc} = 1$) and each particle was scattered only once per timestep ($N_{cp} = 1$), the variance of the scattering angle distribution reduces to

$$\langle \delta^2 \rangle = (\frac{m_1 v_{z_{th}}}{p_{cm}})^2 \frac{v_{z_{th}}}{v_{cm}} \nu \Delta t. \tag{4}$$

In general, the value of the collision frequency ν which is input to the code will not be equal to the "physical" collision frequency which would be calculated from the other input parameters. As stated earlier, the binary collision rate is accelerated so that the the mirror bounce time and the (typically) much longer 90° scattering time are not so disparate as to preclude simulation with available computer resources.

3.1 Transverse Diffusion

.The differential equation which describes the transverse diffusion in velocity space of a beam of charged particles is

$$\frac{d}{dt}(\mathbf{v}(t) - \langle \mathbf{v}(t) \rangle)_{\perp}{}^2 = \nu_{90} v^2(t) \tag{5}$$

where $\mathbf{v}(t)$ is the velocity of a particle in the beam at time t, $\langle \mathbf{v}(t) \rangle$ is the mean velocity of the beam at time t, and ν_{90} is the inverse of the 90° scattering time. The 90° deflection frequency is defined in terms of the mass ratio of the incident and target particles (m_1 and m_2), the energy of the incident particle (E_1), the temperature of the target particles (T_2) and the "basic" collision frequency ν_o as[7]

$$\nu_{90} \equiv 2[\mu(x)(1 - \frac{1}{2x}) + \mu'(x)]\nu_o \tag{6}$$

where the Maxwell integral is defined as

$$\mu(x) \equiv \frac{2}{\sqrt{\pi}} \int_0^x \sqrt{t} e^{-t} dt \tag{7a}$$

with

$$x \equiv (\frac{m_2}{m_1} \frac{E_1}{T_2}). \tag{7b}$$

The diagnostic that was used to study the rate of transverse diffusion of a beam is the time history of the sine of the mean velocity pitch angle

$$\langle sin^2 \phi(t) \rangle = \frac{1}{N_{sp}} \sum_{i=1}^{N_{sp}} (\frac{v_{\perp,i}^2(t)}{v_i^2(t)}) \tag{8}$$

12

where $\phi(t)$ is the pitch angle between the incident beam velocity and the velocity at time (t). If we assume that only small-angle collisions are possible, then for a time $t \ll \tau_o$, the perpendicular velocity component of the i-th particle is given by

$$v_{\perp i}(t) \equiv v_{\perp i}(k\Delta t) \simeq \sum_{it=1}^{k} v_o sin(\delta\theta)_{it}$$

$$\simeq \sum_{it=1}^{k} v_o(\delta\theta)_{it} = v_o \sum_{it=1}^{k}(\delta\theta)_{it} \tag{9a}$$

where $\delta\theta_{it}$ is the angle that the particle is scattered through at timestep it. The speed of the i-th particle is given by

$$v_i(t) \equiv v_i(k\Delta t) \simeq v_o \tag{9b}$$

where v_o is the initial beam velocity. Squaring (9a) gives

$$v_{\perp i}^2(t) \simeq v_o^2(\sum_{it=1}^{k}(\delta\theta)_{it})^2 \simeq v_o^2[\delta\theta_1^2 + \delta\theta_2^2 + \ldots + \delta\theta_k^2]$$

$$\simeq v_o^2 k \langle \delta^2 \rangle \tag{10}$$

where the cross-timestep terms cancel since the scattering angle is uncorrelated with time and $\langle \delta^2 \rangle$ is the variance of the distribution of scattering angles. Substituting (9b) and (10) into (8) yields

$$\langle sin^2\phi(t) \rangle \simeq \frac{1}{N_{sp}} \sum_{i=1}^{N_{sp}} k \langle \delta^2 \rangle \simeq k \langle \delta^2 \rangle. \tag{11}$$

Therefore, the sine squared of the mean velocity pitch angle should vary linearly with the number of timesteps, for times short compared to the basic collision time. The slope of the line should be the variance $\langle \delta^2 \rangle$.

Another check on the accuracy of the model is the large-time asymptotic limit of the $\langle sin^2\phi(t)\rangle$ diagnostic. For times $t \gg \tau_{90}$, where τ_{90} is the 90° scattering time, the initially one-dimensional beam should become isotropic in three-dimensional velocity space. At that point $v_\perp^2 = 2v_\parallel^2$, and since $v^2 = (v_\perp^2 + v_\parallel^2) = 3v_\parallel^2$, then as $t \to \infty$

$$\langle sin^2\phi(t)\rangle \to \langle \frac{v_\perp^2}{v^2}\rangle \to \frac{2}{3}. \tag{12}$$

A nonrelativistic simulation which has an axial electron beam of energy $E_1 = 50$ eV incident upon a three-dimensional, isotropic ion Maxwellian distribution of temperature $T_2 = 1$ eV, with a large mass ratio $m_i/m_e = m_2/m_1 = 1000$ is used to study transverse diffusion. Only unlike-particle (e-i) collisions were performed. Using these values, the variable $x = 5 \times 10^4$, such that $\mu(x) = 1$ and $\mu'(x) = 0$ (see [7], page 178). Equation (6) then gives $\nu_{90} \simeq 2\nu_o$. In practice, the value of ν_o in (6) is replaced by one-half of the input accelerated collision frequency $\nu/2$. For this simulation, the value $\nu\Delta t = 2.5 \times 10^{-3}$ was used, and the ratios $m_1 v_{z_{th}}/p_{cm} \simeq 1$ and $v_{z_{th}}/v_{cm} \simeq 1$. Therefore equation (4) yields $\langle \delta^2\rangle \simeq \nu\Delta t$, such that $\langle sin^2\phi(k\Delta t)\rangle_e \simeq 2.5 \times 10^{-3}k$.

Figure 3 shows the time history of $\langle sin^2\phi(t)\rangle$ for both the electrons (a) and ions (b). The dashed line on the electron time history plot has a slope equal to $\langle \delta^2\rangle$. Note that the time history curve asymptotes to this line for $t \lesssim 2.0 \times 10^{-7}$ sec. A detailed study of the linearity of $\langle sin^2\phi(t)\rangle_e$ for times less than this shows that the difference between the theoretical and calculated results is $\leq 6.69\%$ through $k = 30$ timesteps ($t = 6.0 \times 10^{-8}$ sec). Therefore, the effective 90° scattering time for this

Electron Mean-Square V-Vz Angle History

a)

Time (sec)
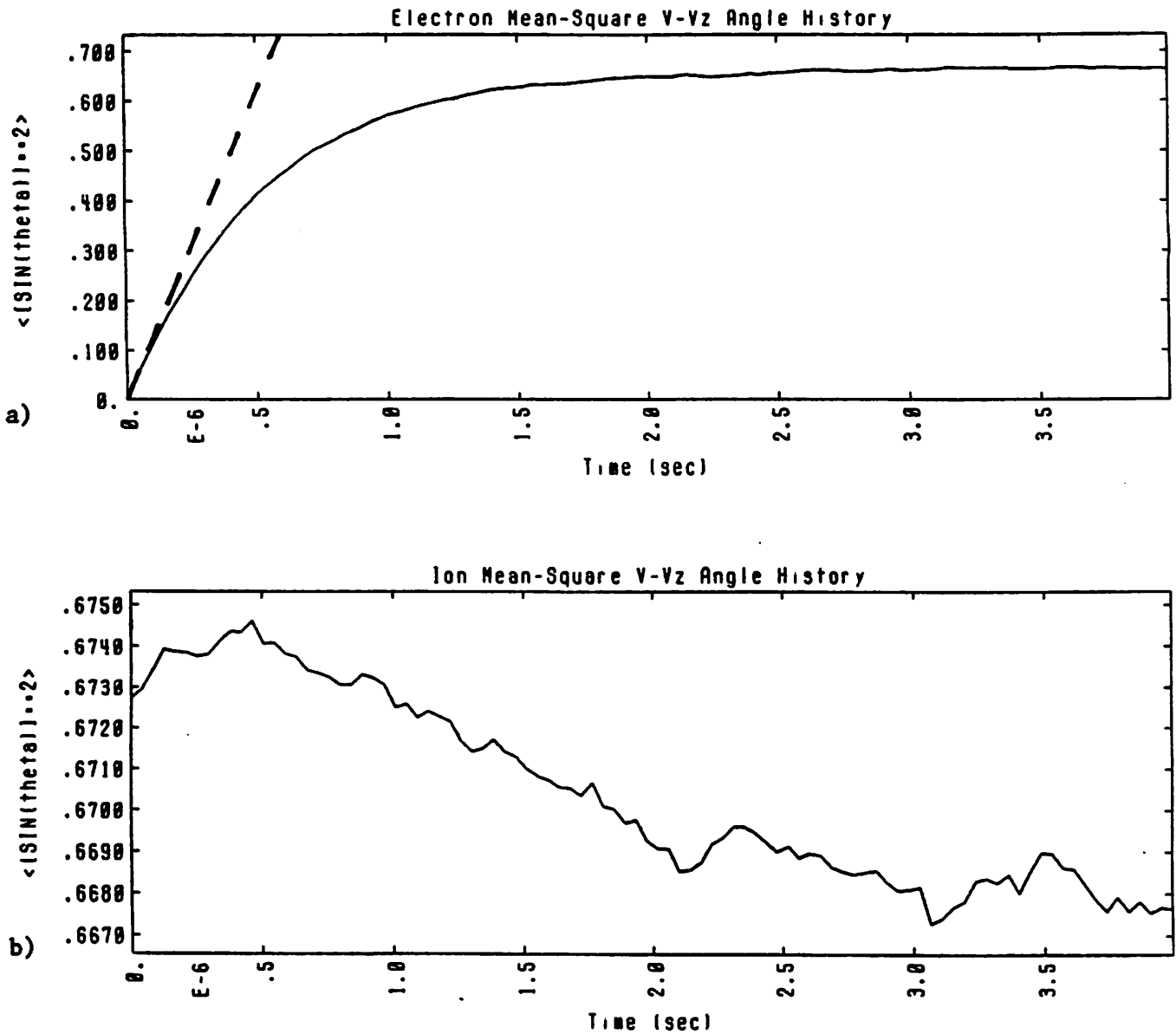
Ion Mean-Square V-Vz Angle History

b)

Time (sec)

Figure 3. Scattering angle time histories of a) electrons
and b) ions for the case of an electron beam ($E_1 = 50$ eV)
incident upon ions ($T_2 = 1$ eV). The mass ratio is m_i/m_e
$= 1000$. Only e-i collisions were performed. The dashed line
on the electron plot has a slope of $\langle \delta^2 \rangle$.

simulation is given by $\tau_{90} \simeq \Delta t/(\nu \Delta t) = (2.0 \times 10^{-9} \text{ sec}/2.5 \times 10^{-3}) = 8.0 \times 10^{-7}$ sec. Note also that for large times, the $\langle sin^2\phi(t)\rangle_e$ time history curve asymptotes to $\sim \frac{2}{3}$. A closer look at the data shows that at timestep $k = 1995$ ($t = 3.99 \times 10^{-6}$ sec), the value of $\langle sin^2\phi(t)\rangle_e = 0.6621$, which varies from the theoretical asymptotic limit by only 0.68%.

At this point a word regarding the statistical accuracy of these simulations is in order. For a simulation involving $N_{sp} = 6400$ particles, the minimum statistical error that is to be expected for an ensemble averaged quantity (such as $\langle sin^2\phi \rangle$) is given by

$$\sigma = \pm\sqrt{\frac{1}{N_{sp}}} = \pm\sqrt{\frac{1}{6400}} = \pm\frac{1}{80} = \pm1.25\%. \qquad (13)$$

The percent differences in the values of $\langle sin^2\phi(t)\rangle_e$ for $k \lesssim 10$ timesteps (small time asymptote) and for $k \simeq 2000$ timesteps (large time asymptote) are within the limits of the statistical error.

Figure 3b displays a small decrease ($\simeq 8\%$) in the value of $\langle sin^2\phi(t)\rangle_i$ with time. This indicates that the ion velocity pitch angle is decreasing with time, such that the ratio $\langle v_{\parallel}/v\rangle_i$ increases with time. The ion velocity-space ($v_{\parallel}$ vs $v_{\perp}$) density contour plot for this simulation at $k = 2000$ timesteps exhibits a slight elongation along the positive $v_{\parallel}$ direction, which is the direction of propagation of the electron beam. This indicates that while the perpendicular velocity distribution function remained Maxwellian, the axial distribution function has been modified by the transfer of low axial velocity particles to the positive $v_{\parallel}$ tail of the distribution.

This is attributable to the transfer of axial momentum from the beam electrons to the ions during scattering events, as illustrated by equation (3).

To check the rate of transverse diffusion in the relativistic limit, the above simulation was repeated with an axial electron beam energy of $E_1 = 500$ keV instead of $E_1 = 50$ eV. All other input parameters were the same and only unlike-particle (e-i) collisions were performed. In this case the ratio of $m_1 v_{z_{th}}/p_{cm} = 0.6726$, while the ratio $v_{z_{th}}/v_{cm} = 0.9992$. With $\nu \Delta t = 2.5 \times 10^{-3}$, equation (4) gives $\langle \delta^2 \rangle = 1.13 \times 10^{-3}$. The same analysis that was applied to the nonrelativistic simulation is applied here. In the small-time asymptotic limit, the curve of $\langle sin^2 \phi(k\Delta t) \rangle_e$ should be a line with slope 1.13×10^{-3} per timestep. The data indicates that the curve is linear to within 3.45% through $k = 30$ timesteps ($t = 6.0 \times 10^{-8}$ sec), with an average slope of 1.12×10^{-3} per timestep. The large-time asymptotic limit of $\langle sin^2 \phi(t) \rangle_e$ is found to be 0.6389 at timestep $k = 1995$ ($t = 3.99 \times 10^{-6}$ sec), which is within 4.17% of the theoretical value of $\frac{2}{3}$. Therefore, in both the small-time and large-time limits, the difference between the theoretical and simulated rates of transverse diffusion of charged particles in a beam is close to the statistical uncertainty, for both relativistic and nonrelativistic particles.

3.2 Slowing Down

The differential equation that describes the slowing down of charged particles in a beam is

$$\frac{d}{dt}\mathbf{v}(t) = -\nu_s \mathbf{v}(t) \tag{14}$$

where $\mathbf{v}(t)$ is the velocity of a particle in the beam at time t, and ν_s is the slowing down frequency, which is defined in terms of the mass ratio, Maxwell integral and basic collision frequency to be

$$\nu_s \equiv (1 + \frac{m_1}{m_2})\mu(x)\nu_o. \qquad (15)$$

Solving (14) for the i-th particle of an initially axial beam gives

$$v_{\|i}(t) = v_{\|i}(k\Delta t) = v_{\|i}(0)exp[-\nu_s t]. \qquad (16)$$

At time $t = \tau_s = 1/\nu_s$, known as the slowing down time, this becomes $v_{\|i}(\tau_s) = v_{\|i}(0)e^{-1} = 0.3679v_{\|i}(0)$. The time history of the mean axial particle velocity of an initially axial beam, ie.

$$\langle v_{\|}(t) \rangle = \frac{1}{N_{sp}} \sum_{i=1}^{N_{sp}} v_{\|i}(t), \qquad (17)$$

will be used as the diagnostic to check the slowing-down rate in the beam.

The nonrelativistic simulation which was used to determine the 90° scattering time is also used here, hence only unlike-particle (e-i) scattering is performed. Figure 4 shows the time histories of the mean axial electron (a) and ion (b) velocities. The data indicates that the e-folding slowing-down time, where $v_{\|}(\tau_s) = 0.3679(2.96 \times 10^8)$ cm/sec $= 1.09 \times 10^8$ cm/sec, is $\tau_s = 1.54 \times 10^{-6}$ sec. Since the mass ratio $m_e/m_i = m_1/m_2 = 10^{-3}$, equation (15) yields $\nu_s = 1.001\nu_o \simeq \nu/2$, such that $\tau_s \simeq 2\tau_{90}$, where as in the previous section, ν_o has been replaced by ν. Using the value of τ_{90} determined in the previous section, the expected theoretical value of $\tau_s = 1.6 \times 10^{-6}$ sec. The difference between the theoretical and simulation results is 3.47%.
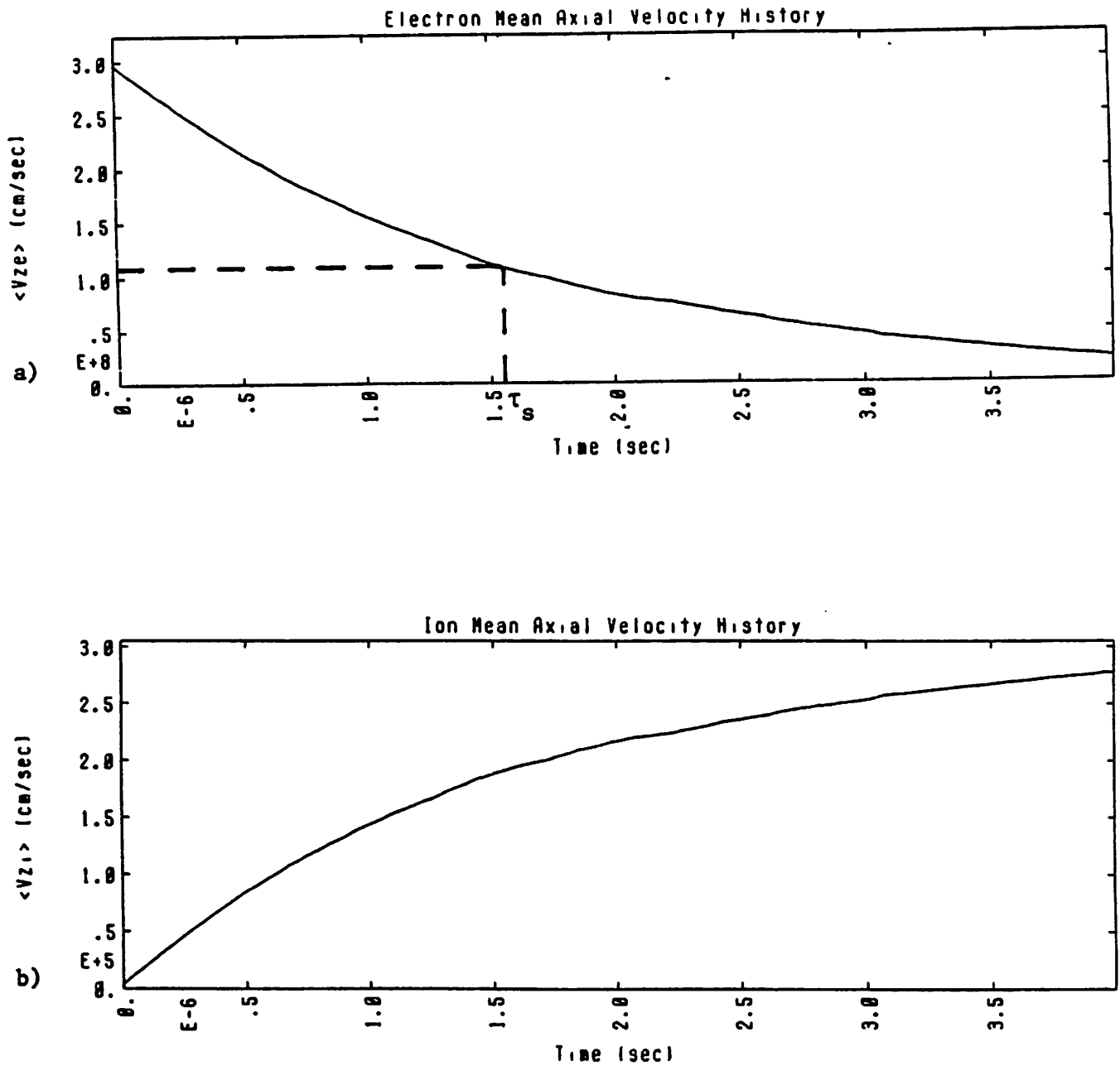
Figure 4. Mean axial velocity time histories of a) electrons and b) ions for the case on an electron beam ($E_1 = 50$ eV) incident upon ions ($T_2 = 1$ eV). The mass ratio is $m_i/m_e = 1000$. Only e-i collisions were performed. The slowing down time is shown on the electron plot.

3.3 Energy Loss

The differential equation which describes the transfer of energy from a high energy test particle to a lower energy field particle is

$$\frac{d}{dt}E_1(t) = -\nu_\epsilon E_1(t) \tag{18}$$

where ν_ϵ is the inverse of the energy-loss time. For a large mass ratio in a nonrelativistic simulation

$$\nu_\epsilon \equiv 2[(\frac{m_1}{m_2})\mu(x) - \mu'(x)]\nu_o. \tag{19}$$

As in the previous sections, $\mu(x)$ is the Maxwell integral and ν_o is the basic collision frequency.

The electron and ion kinetic energy time history plots are used to check the energy transfer rate between an electron beam and a Maxwellian ion distribution. The total kinetic energy of the electron and ion species at time t is given by

$$E_c(t) = \sum_{j=1}^{N_{sp_e}} (\gamma_j - 1)m_{e_o}c^2 \tag{20a}$$

and

$$E_i(t) = \sum_{j=1}^{N_{sp_i}} (\frac{\mathbf{p}_{z_j}^2}{2m_i} + \mu_j B) \tag{20b}$$

respectively, where $\gamma_j \equiv [1 - (v_j/c)^2]^{-1/2}$, with c the speed of light, m_{e_o} is the electron rest mass, $\mathbf{p}_{z_j}$ is the ion axial momentum and μ_j is the ion magnetic moment.

The kinetic energy which is transferred from the incident particle to the target particle during the scattering event, as described by Equation 12.55 of [4], is

$$\Delta E_1 = -(\frac{m_2 \mathbf{p}_{1L}^2 c^4}{E'^2})\frac{\theta'^2}{2} \tag{21a}$$

where $\mathbf{p}_{1L}$ is the incident particle momentum in the target-particle-at-rest frame, and $E'^2 \equiv (m_1^2 c^4 + m_2^2 c^4 + 2m_2 c^2 \sqrt{\mathbf{p}_{1L}^2 c^2 + m_1^2 c^4})$. In the nonrelativistic limit, this reduces to

$$\Delta E_1 = -\frac{m_2(m_1 \mathbf{v}_{1L})^2}{(m_1 + m_2)^2}\frac{\theta'^2}{2} = -E_1 \frac{m_1 m_2}{(m_1 + m_2)^2}\theta'^2$$

$$\simeq -E_1 \frac{m_1 m_2}{(m_1 + m_2)^2}\langle \delta^2 \rangle. \tag{21b}$$

For nonrelativistic simulations with $m_2/m_1 \gg 1$ and $E_1/T_2 > 1$, it has been shown that $\langle \delta^2 \rangle \simeq \nu \Delta t$, such that

$$\frac{\Delta E_1}{\Delta t} \simeq -E_1 \frac{m_1 m_2}{(m_1 + m_2)^2}\nu \tag{21c}$$

which in the limit $\Delta t \to 0$ reduces to the differential equation

$$\frac{d}{dt}E_1(t) = -[\frac{m_1 m_2 \nu}{(m_1 + m_2)^2}]E_1(t). \tag{21d}$$

If the effective (accelerated) energy-loss frequency is defined as

$$\nu_\epsilon \equiv [\frac{m_1 m_2}{(m_1 + m_2)^2}]\nu \tag{22}$$

then the solution of (21d) for the kinetic energy of the particles in the beam at time t is

$$E_1(t) = E_1(0)exp[-\nu_\epsilon t]. \tag{23a}$$

Note that for $m_2/m_1 \gg 1$, $\nu_\varepsilon \simeq (m_1\nu/m_2)$,so

$$E_1(t) \simeq E_1(0)exp[-(\frac{m_1\nu}{m_2})t]. \qquad (23b)$$

The inverse of the time constant $m_2/m_1\nu$ in equation (23b) is equivalent to the energy-loss rate of equation (19), with ν_o replaced by $\nu/2$, and with $\mu(x) \to 1$ and $\mu'(x) \to 0$ for values of $x \equiv (m_2E_1/m_1T_2) \gtrsim 6$ (see [7], page 178).

At time $t = \tau_\varepsilon = 1/\nu_\varepsilon$, known as the energy-loss time, one can see that $E(\tau_\varepsilon) = E(0)e^{-1} = 0.3679E(0)$. Figure 5 shows the time histories of the total species kinetic energy for the electrons (a) and the ions (b) from a nonrelativistic simulation for which the mass ratio $m_2/m_1 = m_i/m_e = 12$ and the energy ratio $E_1/T_2 = E_e/T_i = 50$. Only unlike-particle (e-i) scattering is performed. For this simulation $\tau_\varepsilon \simeq 12\tau_{90} \simeq 9.6 \times 10^{-6}$ sec.

It is important to note that equation (23a) may only be accurate for times much less than τ_ε. For instance, the rate of energy transfer between an electron beam and a Maxwellian ion distribution is likely to be different than that between electron and ion Maxwellian distributions, even if the ratio E_e/T_i is the same. This is a consequence of the fact that the energy equilibration rate for a beam and a Maxwellian distribution is not the same as that for two interacting Maxwellian distributions. To check the energy-loss rate, the ratio $E_e(t)/E_e(0)$ from the simulation is compared to the value of $exp[-t/\tau_\varepsilon]$, in which the theoretical value of $\tau_\varepsilon = 9.6 \times 10^{-6}$ sec was used. The simulation results agree with the theoretical predictions to within 1.34% (which is near the limit of the statistical accuracy of the simulation) through $k = 216$ timesteps ($t = 4.32 \times 10^{-7}$ sec $\ll \tau_\varepsilon$). As the
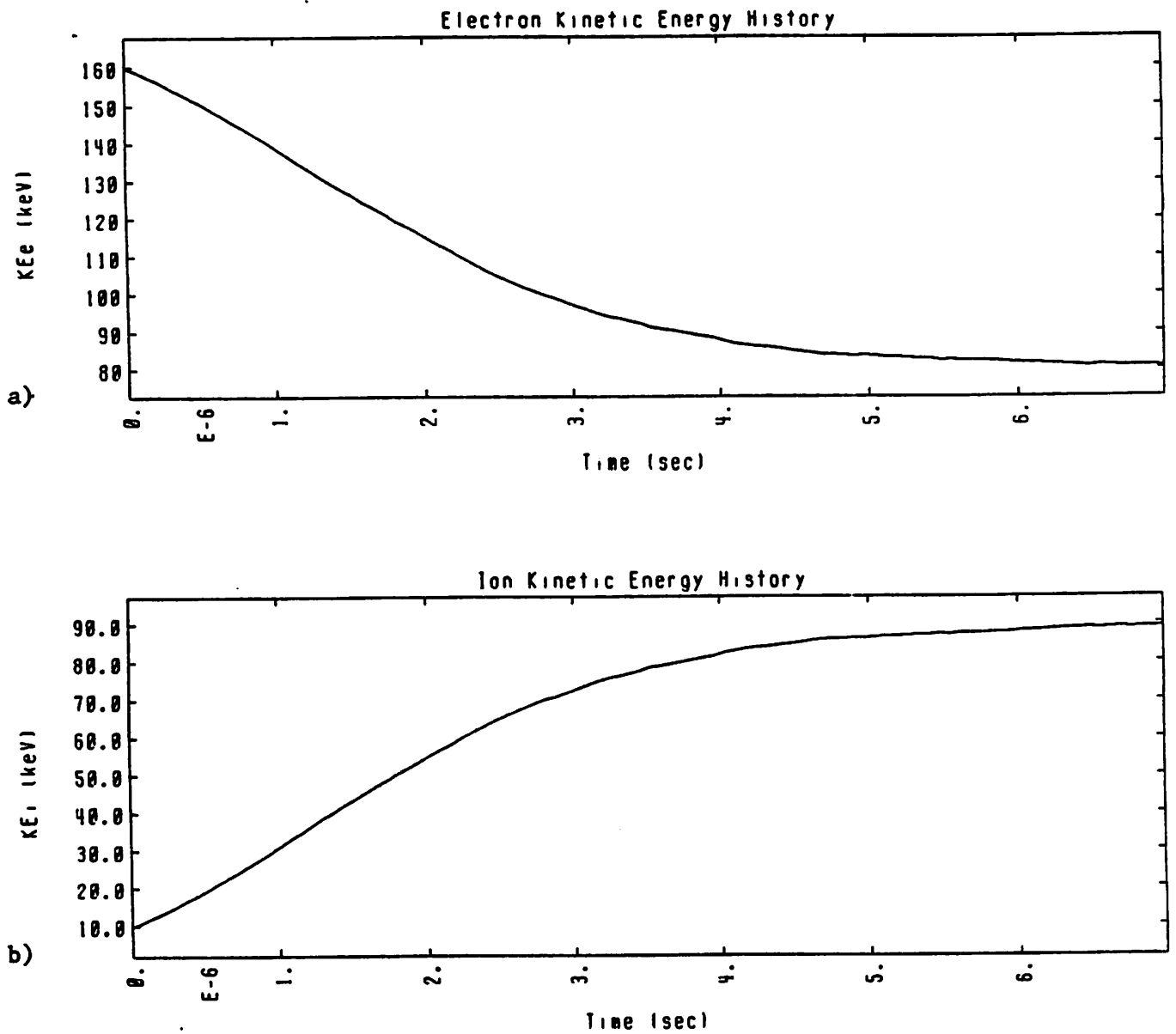
Figure 5. The total kinetic energy time histories of a) electrons and b) ions for the case of an electron beam ($E_1 = 50$ eV) incident upon ions ($T_2 = 1$ eV). The mass ratio is $m_i/m_e = 12$. Only e-i collisions were performed. The energy loss time is shown on the electron plot.

simulation proceeds in time, the difference continues to grow, and approaches 20% at $k = 1400$ timesteps ($t = 2.8 \times 10^{-6}$ sec).

A comparison of Figures 5a and 5b shows that the energies of the two species have not equilibrated after $k = 3500$ timesteps ($t = 7.0 \times 10^{-6}$ sec), although the kinetic energy of each of the species has leveled off. Note however, that after $t \simeq 5.0 \times 10^{-6}$ sec, the ions have a greater total kinetic energy than do the electrons: the electron and ion kinetic energies have overshot the equilibration energy value of 85 keV. Although this seems contradictory to the laws of thermodynamics, it may be accounted for by looking at the rates of the various processes that are occurring during the simulation. For nonrelativistic incident electrons and target ions (with $x \gg 1$) it can be shown[7] that the characteristic times for the processes of interest have the following relative magnitudes

$$\tau_{90} : \tau_s : \tau_\epsilon : \tau_{eq} = 1 : 2 : (m_i/m_e) : (E_e m_i/2T_i m_e) \tag{24}$$

where τ_{eq} is the energy equilibration time. In this case, the relative magnitudes are $1 : 2 : 12 : 300$. With $\tau_{90} = 8.0 \times 10^{-7}$ sec, the simulation encompasses $8.75\tau_{90}$, $4.38\tau_s$, $0.73\tau_\epsilon$ and only $0.03\tau_{eq}$, based upon the initial input parameters. Therefore, a simulation several times longer than the one that was performed would be necessary for the energy of the two species to equilibrate.

As an additional check on the validity of the simulation, the entropy of each of the species was followed during the simulation

$$S(t) \equiv \int_{v_\parallel} \int_{v_\perp} f(v_\parallel, v_\perp) log[f(v_\parallel, v_\perp)] dv_\perp dv_\parallel. \tag{25}$$

The electron entropy increases rapidly from zero at the start of the simulation (the beam is a delta function in velocity space, hence the electrons are perfectly ordered and the entropy is zero) due to transverse diffusion of the beam in velocity space. This is followed by a small increase over approximately a 90° deflection time, after which the entropy remains constant. The ion entropy increases gradually from the non-zero value associated with the bi-Maxwellian distribution, and then remains constant for the second half of the simulation. Figure 6 shows the time histories of the electron (a), ion (b) and combined or total entropy (c). Note that the total entropy either inceases or remains constant (to within statistical fluctuations). Since the binary collision algorithm conserves total kinetic energy, the simulation obeys both the First and Second Laws of Thermodynamics.

3.4 Additional Relaxation Processes

Several additional simulations were made to study the specific relaxation processes that are analyzed by Takizuka and Abe in [3]. These processes are the relaxation of a drifting Maxwellian distribution, the equilibration of two Maxwellian distributions with different temperatures and the isotropization of a bi-Maxwellian distribution with different axial and perpendicular temperatures.

3.4.1 Relaxation of a Drifting Maxwellian Distribution

For these simulations, the electrons and ions have a single temperature ($T = T_\parallel = T_\perp$). In addition, the electrons have an initial net drift velocity $v_{d_{e_o}}$ in the axial direction. The ion temperature is chosen such that $T_{i_o} \ll (m_i/m_e)T_{e_o}$. Equation (14) describes the time variation of the mean electron velocity ($v(t) \equiv \langle v(t) \rangle_e$),
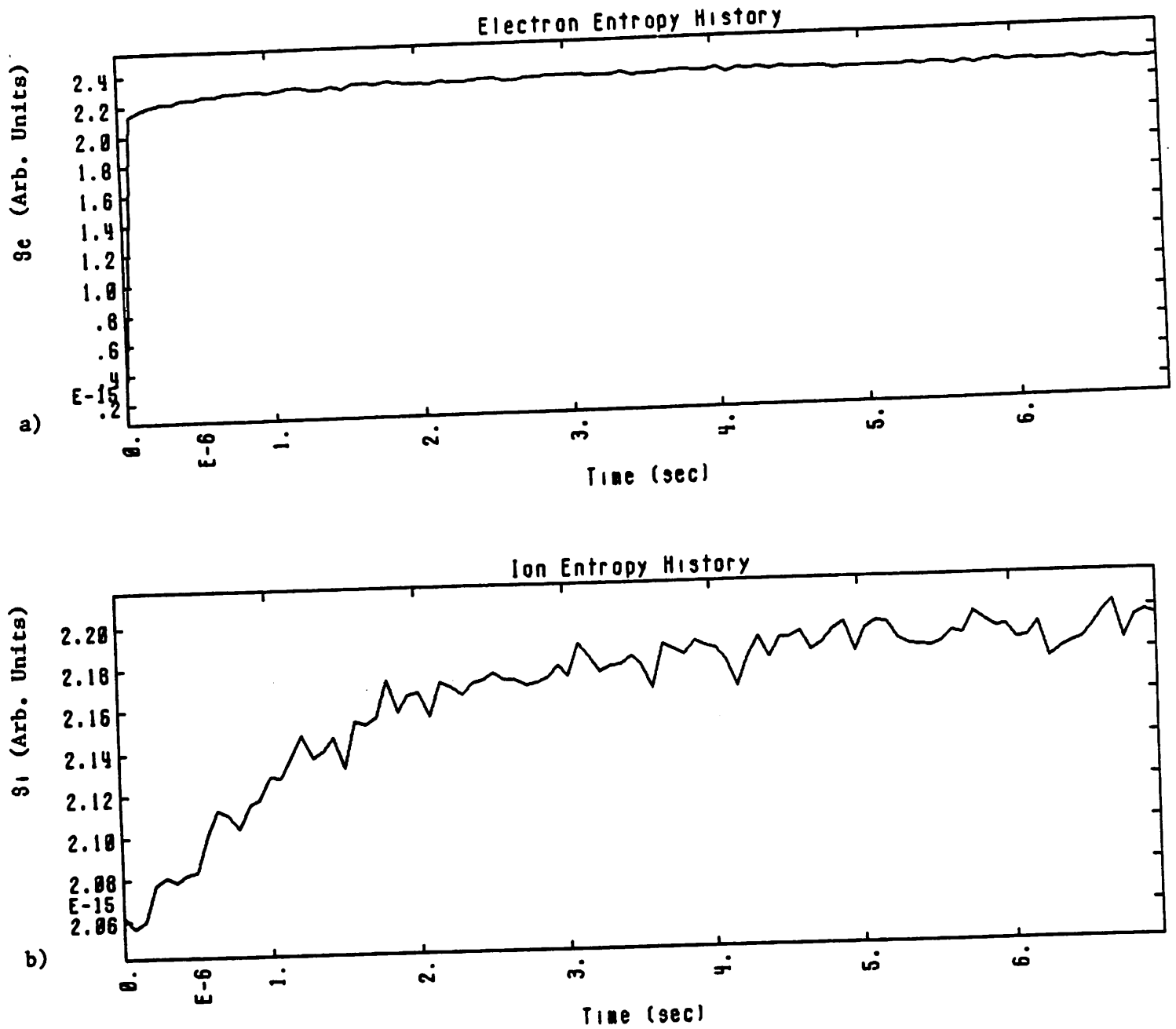
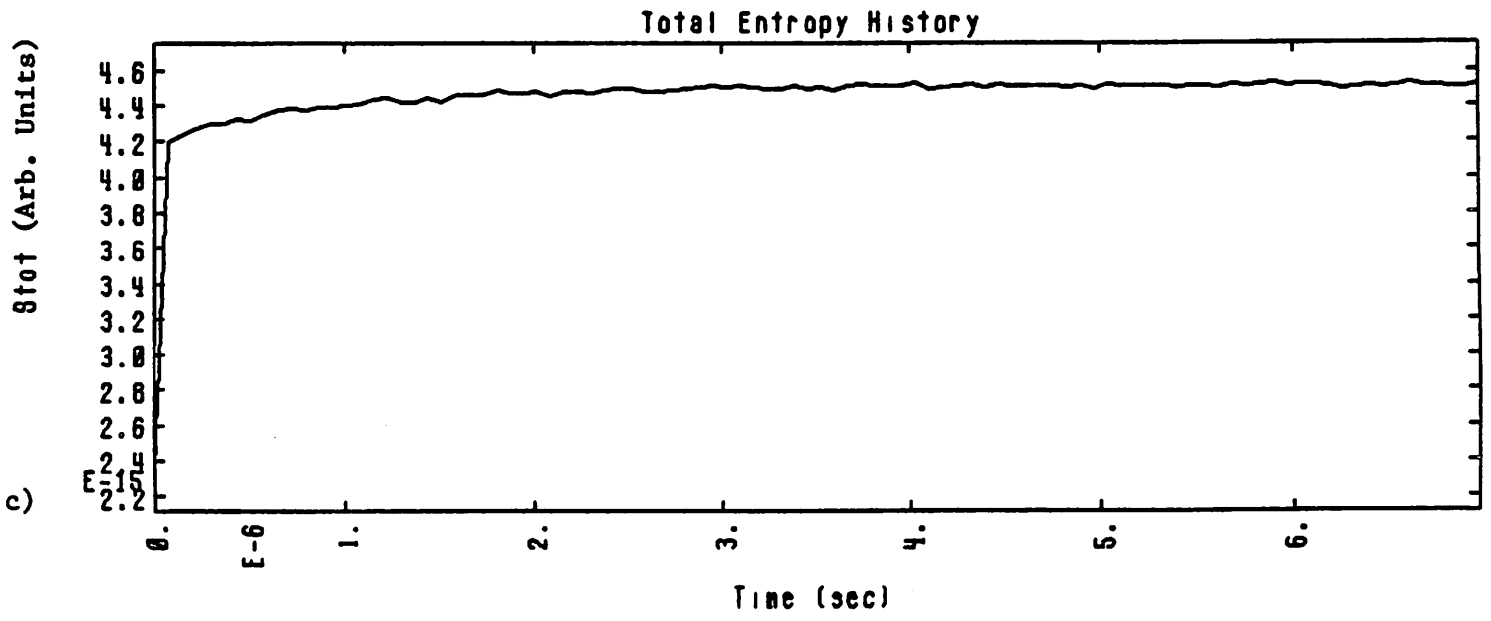Figure 6. Entropy time histories of the a) electrons, b) ions and c) electrons plus ions (combined or total entropy).

Figure 6. (continued)

however the slowing down frequency for this specialized process is given by

$$\nu_s = \frac{1}{4}\mu(x')(x')^{-3/2}\nu_o \tag{26}$$

where $x' \equiv (\varepsilon/T_{e_o})$, with $\varepsilon \equiv m_e v_{d_{eo}}^2/2$, while μ is the Maxwell integral and ν_o is the basic collision frequency.

The mass ratio for these simulations is $m_i/m_e = 1836$, the ion temperature is $T_{i_o} = 1$ eV and the electron temperature is $T_{e_o} = 50$ eV. Only unlike-particle (e-i) scatterings are performed. The diagnostic used to study this process is the time history of the electron drift velocity ratio

$$\frac{v_{d_e}(t)}{v_{d_{eo}}} = \frac{1}{v_{d_{eo}} N_{sp_e}} \sum_{i=1}^{N_{sp_e}} v_{\parallel i}(t). \tag{27}$$

Figure 7 shows this time history plots for (a)$\varepsilon = T_{e_o}/2$, (b)$\varepsilon = T_{e_o}$ and (c)$\varepsilon = 2T_{e_o}$. The dashed lines on these plots indicate the theoretical predictions of equations (14) and (26). Notice that the agreement is best near the beginning of the simulation, which is to be expected, since the theory is valid only in the small-time asymptotic limit. The data indicates that at $k = 800$ timesteps ($t = 1.6 \times 10^{-6}$ sec), the difference between the theoretical and simulation values is 2.87% for run (a), 2.45% for run (b) and 1.70% for run (c). The final time of these simulations corresponds to $1.25\tau_o$, where the basic collision time $\tau_o = 1/\nu_o = 1.6 \times 10^{-6}$ sec.

3.4.2 Energy Equilibration of Two Maxwellian Distributions

The electrons and ions in these simulations have single temperature Maxwellian distributions, however initially $T_{e_o} \neq T_{i_o}$. Several combinations of mass ratio and
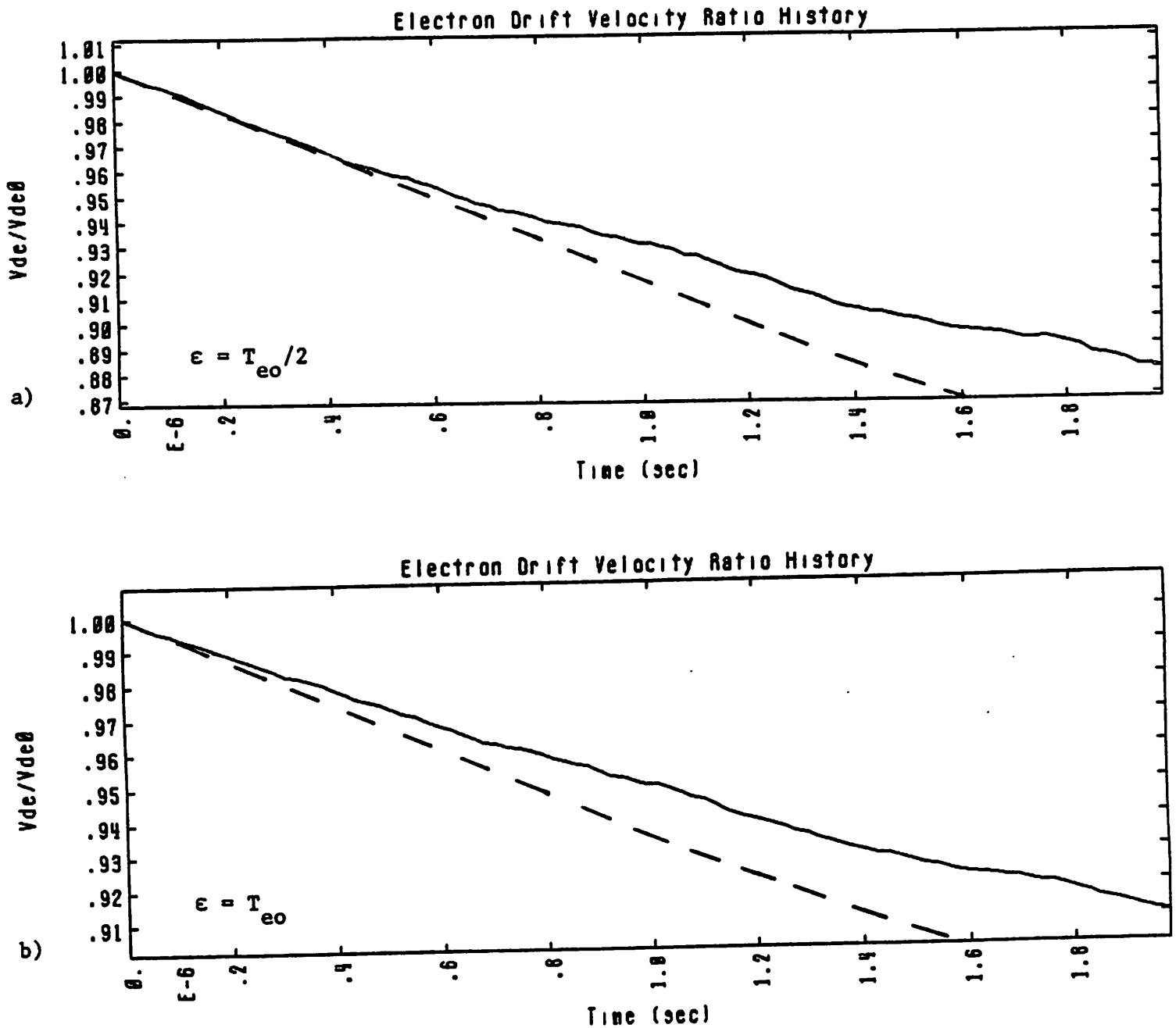
Figure 7. Relaxation of a drifting electron Maxwellian velocity distribution. The temperatures are $T_1 = 50$ eV for the electrons and $T_2 = 1$ eV for the ions. The mass ratio is $m_i/m_e = 1836$. Only e-i collisions were performed. [a) $\epsilon = T_{e_o}/2$; b) $\epsilon = T_{e_o}$; c) $\epsilon = 2T_{e_o}$]
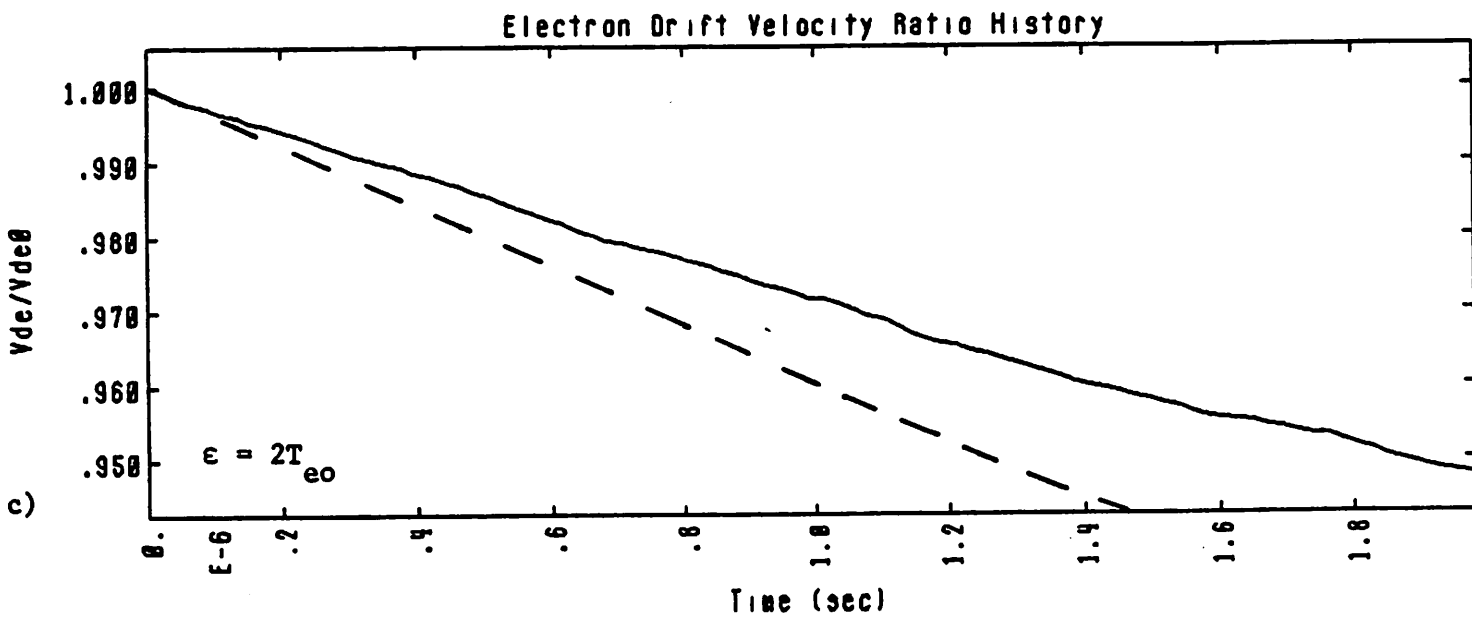
Figure 7. (continued)

temperature ratios were studied. The differential equation that describes this temperature relaxation process is

$$\frac{d}{dt}(T_i(t) - T_e(t)) = -\nu_{teq}(T_i(t) - T_e(t)) \tag{28}$$

where ν_{teq} is the inverse of the temperature equilibration time, and is defined by

$$\nu_{teq} = \frac{2}{3\sqrt{\pi}}\frac{m_e}{m_i}(1 + \frac{1}{x''})^{-3/2}\nu_o \tag{29}$$

where $x'' \equiv (m_i T_e / m_e T_i)$.

Only unlike-particle (e-i) scatterings are performed in these simulations. The diagnostic that is used to study the temperature equilibration rate is the time history of $(T_e(t) - T_i(t))/(T_{e_o} - T_{i_o})$, where the temperature at time t in a system which has 2 degrees of freedom ($\parallel$ and $\perp$) is defined in terms of individual particle velocities as

$$T(t) \equiv \frac{m}{2N_{sp}}\sum_{i=1}^{n_{sp}}[v_{\parallel i}^2(t) + v_{\perp i}^2(t)]. \tag{30}$$

The results of three simulations are shown in Figure 8. The simulation shown in Figure 8a used a mass ratio $m_i/m_e = 4$ and temperature ratio $T_{e_o}/T_{i_o} = 2$, while Figure 8b is for a simulation with the same mass ratio, but a temperature ratio $T_{e_o}/T_{i_o} = \frac{1}{2}$. The mass ratio used to produce Figure 8c was $m_i/m_e = 16$, with a temperature ratio $T_{e_o}/T_{i_o} = 2$. The dashed lines in these figures are the theoretical predictions of equations (28) and (29). The maximum difference between the theoretical and simulation results is approximately 11.4% for run (a), 5.0% for run (b) and 3.6% for run (c) through $k = 1000$ timesteps ($t = 2.0 \times 10^{-6}$ sec). The
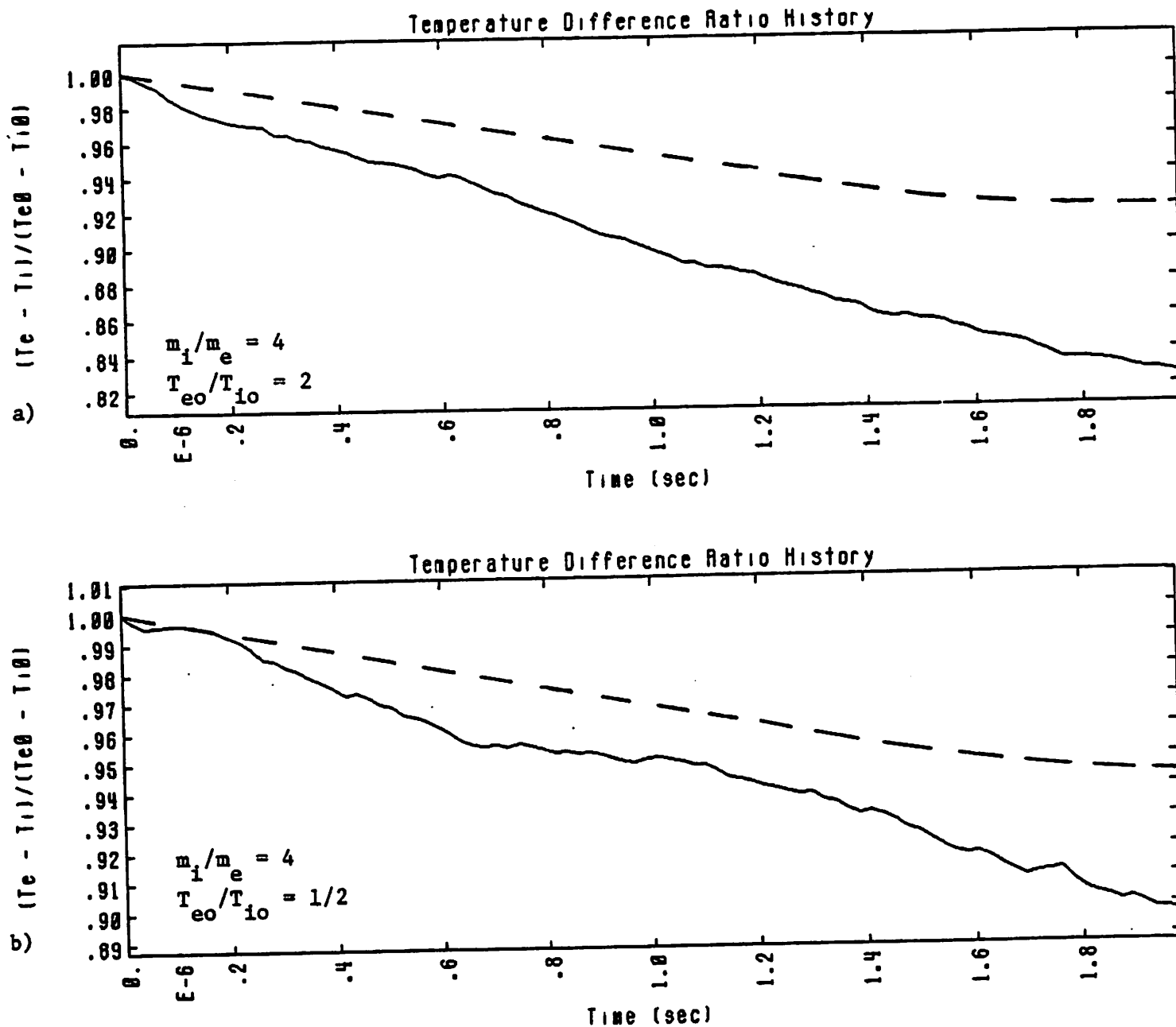
Figure 8. Energy equilibration of two Maxwellian distributions. The electron temperature is $T_1 = 50$ eV. Only e-i collisions were performed. [a) $m_i/m_e = 4$, $T_{e_o}/T_{i_o} = 2$; b) $m_i/m_e = 4$, $T_{e_o}/T_{i_o} = 1/2$; c) $m_i/m_e = 16$, $T_{e_o}/T_{i_o} = 2$]
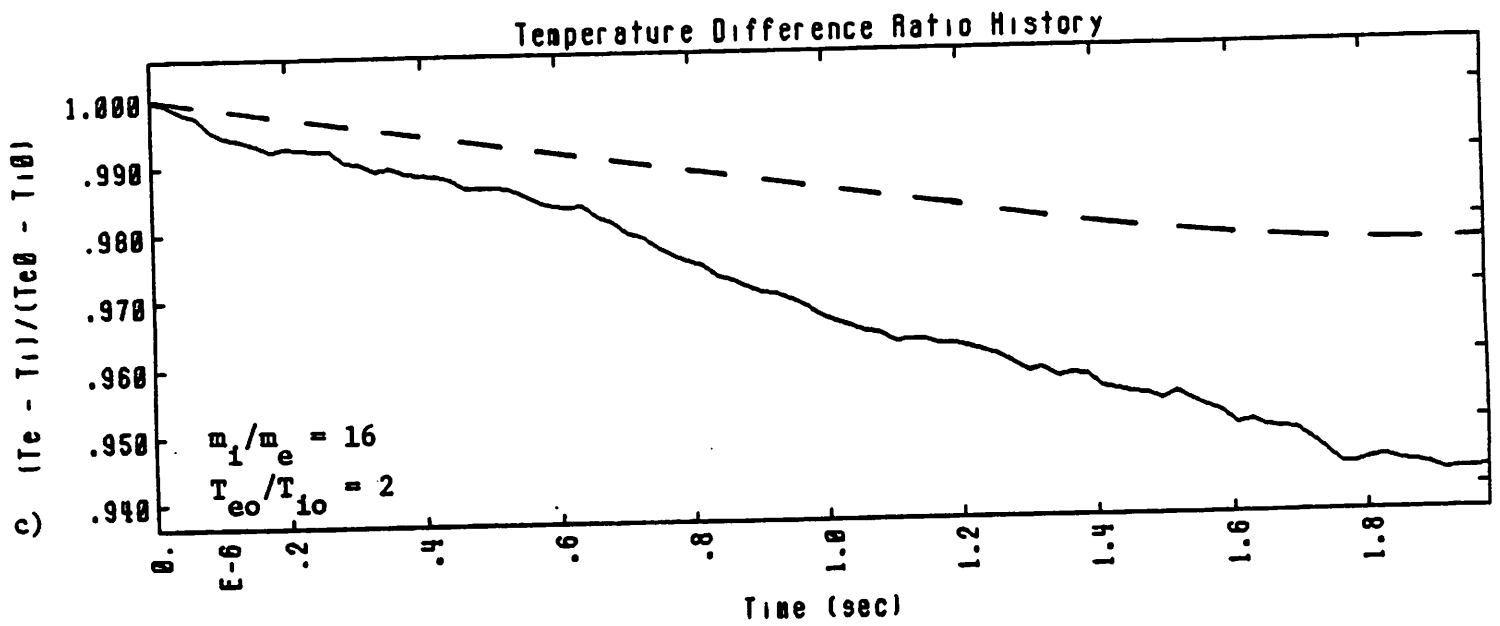
Figure 8. (continued)

data suggests that the agreement with theory increases as the mass ratio increases and the temperature ratio decreases. The reason for the poor agreement at low mass ratios, is that one can no longer assume that $\langle \delta^2 \rangle \simeq 2\nu_o \Delta t k$, or rather that $\nu = 2\nu_o$, as was done previously for the large mass ratio simulations. Therefore, the uncertainty of the value of ν_o that is used in equation (28) limits the accuracy of the theoretical predictions.

3.4.3 Relaxation of a bi-Maxwellian Distribution

To study the rate of isotropization of a bi-Maxwellian temperature distribution with $T_\parallel \neq T_\perp$, a simulation was performed which used an axial to perpendicular temperature ratio for the electrons of $T_{\parallel e_o}/T_{\perp e_o} = 2$, in which only e-e collisions were considered. The characteristic differential equation for isotropization of a bi-Maxwellian distribution is

$$\frac{d}{dt}(T_\parallel(t) - T_\perp(t)) = -\nu_{iso}(T_\parallel(t) - T_\perp(t)) \tag{31}$$

where ν_{iso} is defined by

$$\nu_{iso} \equiv 5\sqrt{\frac{2}{\pi}}\nu_o. \tag{32}$$

The mass ratio for the simulation was $m_i/m_e = 1836$, with a temperature ratio of $T_{\parallel e}/T_i = 50$. The diagnostic for this relaxation process is the time history of $(T_{\parallel e}(t) - T_{\perp e}(t))/(T_{\parallel e_o} - T_{\perp e_o})$. The temperatures at time t are defined by

$$T_{\parallel,\perp}(t) \equiv \frac{m}{2N_{sp}} \sum_{i=1}^{N_{sp}} v_{\parallel,\perp_i}^2(t). \tag{33}$$

The result of the simulation is presented in Figure 9. The dashed line in the figure represents the theoretical prediction obtained by use of equations (31) and (32).
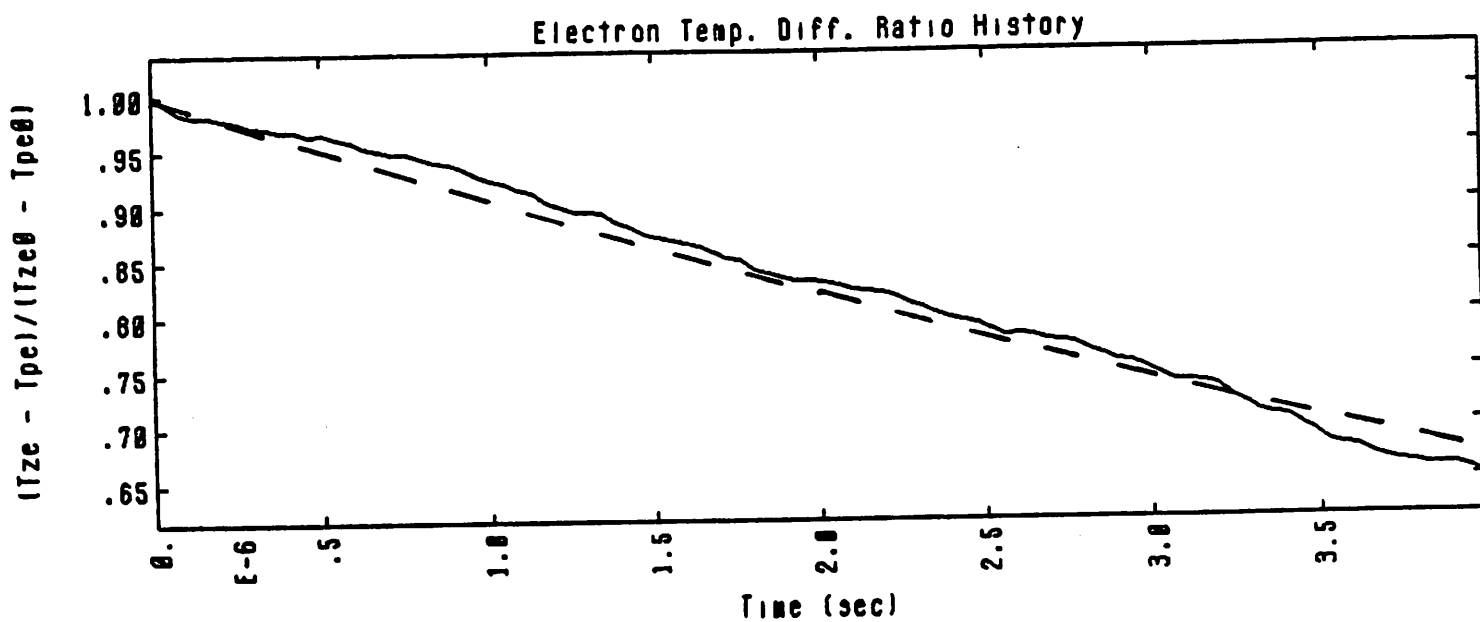
Figure 9. Temperature anisotropy relaxation of a bi-Maxwellian distribution. The temperature are $T_{\parallel_e} = 50$ eV, $T_{\perp_e} = 25$ eV and $T_i = 1$ eV. The mass ratio is $m_i/m_e = 1836$. Only e-e collisions were performed.

Note the oscillation of the simulation result about the theoretical curve. This is the only case in which the two curves do not diverge. The maximum difference between the two curves is $\simeq 3.0\%$.

4. Model Timing and Recommendations for Use

An important goal in our modeling of the collisional interactions of the plasma particles is a computationally efficient resolution of the disparate physical time scales of the plasma processes. The brief description of the model which is presented in Section 2 indicates that it is rather computationally intensive. For instance, the process requires a total of four changes of reference frame for each pair of particles that are scattered. Care must be taken in choosing values for the input parameters $\nu\Delta t$, N_{tc} and N_{cp} such that the collisional phenomena are accurately simulated, while minimizing the number of executions of the collision package.

Code timings for simulations in which the particles are collided every timestep ($N_{tc} = 1$ and $N_{cp} = 1$) show that the binary collision package dominates the other major physics packages, with regard to run time. In this case, the total code run time is approximately 34 microseconds per particle per timestep, of which 24.0 were spent colliding particles. This includes 6.0 microseconds per particle per timestep for each type of like-particle scattering (e-e and i-i), and 12.0 microseconds per particle per timestep for unlike-particle scattering (e-i). (This factor of two comes about because in any given grid cell, the particle lists for e-e and i-i scattering are only half as long as the list for e-i scattering). These timings compare to 7.2 microseconds per particle per timestep for the FORTRAN particle pusher and 15.0 milliseconds per timestep (using the LINPACK matrix inversion package) for the

solution of Poisson's equation in a region with 128 grid cells. The cost of the field solver becomes negligible as the number of particles of each species is increased above 10^4. The collisions, however, account for about 70% of the total run time.

By increasing the value of the parameter N_{tc} above 1, the overall percentage of the code run time that is due to the collision routine is reduced. For example, if the collisions package were executed only every 5-th timestep, the total code run time for those 5 timesteps is about 74 microseconds per particle, of which 24 are required to perform the collisions, so the amount of time spent colliding the particles is reduced to approximately 32% of the total. However, increasing N_{tc} can lead to a violation of the assumption of small-angle scattering, since $\langle \delta^2 \rangle \sim N_{tc}\nu\Delta t/N_{cp}$. The violation of this critical assumption is an important issue that is discussed in detail below.

This binary collision model is rigorous, except for the neglect of Bremsstrahlung radiation damping and the assumption of small-angle scattering. The Bremsstrahlung energy loss is certainly negligible for nonrelativistic collisions, but is the dominant energy loss mechanism for ultrarelativistic collisions.[4] Because the COM scattering angle $\theta' \sim \langle \delta^2 \rangle^{1/2}$, there are three possible ways in which the small-angle assumption could be violated. The first occurs if the COM velocity of the colliding particles is much less than the thermal velocity of the test particle ($v_{cm} \ll v_{z_{th}}$), the second way is if the local to average particle density ratio $n_{loc}/n_{ave} \gg 1$, and the third is due to a large value of the term $N_{tc}\nu\Delta t/N_{cp}$. It is of course possible to have all three factors contribute concurrently. Therefore, safeguards have been installed in the code to ensure that θ' does not exceed 20°. For all cases in which the calculated

values of $\theta' > 20°$, the angle is "clamped" at $20°$ by fixing the value of $\langle \delta^2 \rangle$ at 4.0×10^{-2}.

The third method of violating the small-angle scattering assumption is the only one that is directly controllable. As the value of $N_{tc}\nu\Delta t/N_{cp}$ increases, larger volumes of velocity space have scattering angles which are clamped by the previously described safeguard. To see this, consider a situation in which $n_{loc}/n_{ave} = 1$. In that case

$$\langle \delta^2 \rangle = (\frac{m_1 v_{zth}}{v_{cm}})^2 \frac{v_{zth}}{v_{cm}} \frac{N_{tc}}{N_{cp}} \nu\Delta t. \tag{34a}$$

In order to determine the volume of velocity space that is clamped for a given value of $N_{tc}\nu\Delta t/N_{cp}$, assume that $p_{cm}/m_1 = v_{cm}$, such that

$$\langle \delta^2 \rangle = (\frac{v_{zth}}{v_{cm}})^3 \frac{N_{tc}}{N_{cp}} \nu\Delta t. \tag{34b}$$

Setting $\langle \delta^2 \rangle = 4.0 \times 10^{-2}$ and replacing v_{cm} by v_{clamp} we arrive at

$$\frac{v_{clamp}}{v_{zth}} = (25 N_{tc}\nu\Delta t/N_{cp})^{1/3}. \tag{34c}$$

For $N_{tc}\nu\Delta t/N_{cp} = 2.5 \times 10^{-3}$, the result is that the θ' is clamped for velocities less than or equal to 39.69% of the thermal velocity. This means that only 6.25% of the volume of a sphere in velocity space with radius equal to the thermal velocity has clamped COM scattering angles. Since the code defines Maxwellian distribution functions out to $v_{max} = 4.5v_{th}$, the clamped volume is negligible, but the number of particles inside the clamped volume may not be, depending upon the form of the velocity distribution function. A secondary safeguard was added to the code which alerts the user if $N_{tc}\nu\Delta t/N_{cp} > 2.5 \times 10^{-3}$.

References

[1]   C. K. Birdsall and D. Fuss, *J. Comp. Phys.*, **3**, 494 (1969).

[2]   R. W. Hockney, *J. Comp. Phys.*, **8**, 19(1971).

[3]   T. Takizuka and H. Abe, *J. Comp. Phys.*, **25**, 205(1977).

[4]   J. D. Jackson, **Classical Electrodynamics**, First Edition, Chap. 12, Wiley, New York(1962).

[5]   L. Spitzer, Jr.,**Physics of Fully Ionized Gases**, First Edition, Chap. 5, Interscience, New York(1956).

[6]   G. A. Bird, *Phys. Fluids*, **13**, 2676(1970).

[7]   B. A. Trubnikov, in **Reviews of Plasma Physics**, Vol. 1, 105, Consultant's Bureau, New York(1965).